

## Article

# A Simplified One-Parallel-Element Automatic Impedance-Matching Network Applied to Electromagnetic Acoustic Transducers Driving <sup>†</sup>

João Pedro T. Andrade <sup>1</sup>, Pedro Leon F. C. Bazan <sup>1</sup>, Vivian S. Medeiros <sup>2</sup> and Alan C. Kubrusly <sup>1,\*</sup> 

<sup>1</sup> Center for Telecommunication Studies, Pontifical Catholic University of Rio de Janeiro, Rio de Janeiro 22451-900, Brazil; jp.t.andrade@cpti.cetuc.puc-rio.br (J.P.T.A.)

<sup>2</sup> Department of Mechanical Engineering, São Carlos School of Engineering, University of São Paulo, São Carlos 13566-590, Brazil; viviansuzano@usp.br

\* Correspondence: alan@cpti.cetuc.puc-rio.br

<sup>†</sup> This paper is an extended version of our paper published in Andrade, J.P.T.; Medeiros, V.S.; Kubrusly, A.C. Simplified automatic impedance-matching network for electromagnetic acoustic transducers. In Proceedings of the 2023 7th International Symposium on Instrumentation Systems, Circuits and Transducers (INSCIT), Rio de Janeiro, Brazil, 28 August–1 September 2023.

**Abstract:** Ultrasonic waves generated and received by electromagnetic acoustic transducers (EMATs) are advantageous in non-destructive testing, mainly due to the ability to operate without physical contact with the medium under test. Nevertheless, they present a main drawback of less efficiency, which leads to a lower signal-to-noise ratio. To overcome this, the L-network impedance-matching network is often used in order to ensure maximum power transfer to the EMAT from the excitation electronics. There is a wide range of factors that affect an EMAT's impedance, apart from the transducer itself; namely, the properties of the specimen material, temperature, and frequency. Therefore, to ensure optimal power transfer, the matching network's configuration needs to be fine-tuned often. Therefore, the automation of the laborious process of manually adjusting the network is of great benefit to the use of EMAT transducers. In this work, a simplified one-parallel-element automatic matching network is proposed and its theoretical optimal value is derived. Next, an automatic matching network was designed and fabricated. Experiments were performed with two different EMATs at several frequencies obtaining good agreement with theoretical predictions. The automatic system was able to determine the best configuration for the one-element matching network and provided up to 5.6 dB gain, similar to a standard manual solution and considerably faster.

**Keywords:** EMAT; nondestructive testing; impedance matching; automation



**Citation:** Andrade, J.P.T.; Bazan, P.L.F.C.; Medeiros, V.S.; Kubrusly, A.C. A Simplified One-Parallel-Element Automatic Impedance-Matching Network Applied to Electromagnetic Acoustic Transducers Driving. *Automation* **2023**, *4*, 378–395. <https://doi.org/10.3390/automation4040022>

Academic Editor: Simon Tomažič

Received: 31 October 2023

Revised: 25 November 2023

Accepted: 28 November 2023

Published: 1 December 2023



**Copyright:** © 2023 by the authors. Licensee MDPI, Basel, Switzerland. This article is an open access article distributed under the terms and conditions of the Creative Commons Attribution (CC BY) license (<https://creativecommons.org/licenses/by/4.0/>).

## 1. Introduction

Ultrasonic waves are widely used in nondestructive testing [1,2]. In order to generate ultrasonic waves, different types of transducers can be used, the most common one being the piezoelectric [3]. These transducers require direct contact with the medium under test, either bonded or through a coupling medium, to operate [3–5]. Electromagnetic acoustic transducers (EMATs) present some advantages compared to traditional piezoelectric transducers. They allow more flexibility in generating several types of ultrasonic waves and polarizations and do not require contact to operate on a conductive medium [3,6–8]. EMATs generally consist of a coil underneath a permanent magnet, or a permanent magnet array, and can operate over three coupling mechanisms; namely, Lorentz force, magnetization force, and magnetostriction, in order to generate ultrasonic waves within the medium [3].

The main drawback of EMATs is their low efficiency. Consequently, they usually present a lower signal-to-noise ratio (SNR) than piezoelectric transducers, which can hinder the use of EMATs [9,10]. One way to alleviate this shortcoming is to guarantee maximum

power transmission from the excitation electronics to the transducer [11,12]. The maximum power transfer theorem states that whenever the electric input impedance of the transducer is equal to the complex conjugate of the output impedance of the pulser, maximum power is transferred to the transducer [13]. Even though the pulser's output impedance is usually fixed, because of the transducer impedance, matching is usually designed for a specific EMAT and operating frequency [6,14].

One important factor in the EMAT's design is its electrical impedance, and there are many factors that can affect it. Not only their coil geometry, but also the distance from the coil to the magnet, as explored by Wu et al. [9]. The presence of a backplate between the transducer's components also affects its impedance, as exposed by Wang et al. [15]. Beyond the EMAT itself, the distance from it to a ferrous material, so-called lift-off, also affects the transducer's impedance [10], and so does the temperature [12]. Finally, the excitation frequency affects the EMAT's impedance as well.

One common way to impedance match EMATs is to use the L-network, which is a circuit composed of two reactive lumped elements [16]. However, to be able to impedance match, the inductance or capacitance values of the network's components depend on the pulser and transducer impedances. Because the EMAT impedance is generally not previously known, as it depends on various factors, the impedance-matching process usually consists of sweeping for the network's configurations that provide the maximum signal amplitude [12]. Manually adjusting these configurations is a time-consuming process and subject to human interpretability and errors. Therefore, automation of this process can be of great benefit to EMAT-based inspection systems, not only for time-saving reasons but also to ensure optimal operation with respect to these various factors.

Some works aim to improve EMAT performance by studying the effects of physical changes in the transducers. Wu et al. [9] studied the effect of magnet-to-coil distance on the performance characteristics of EMATs, concluding that the magnet-to-coil distance affects the magnetic flux density and eddy current density at the medium's surface and that, for a specific EMAT, there is an optimal magnet-to-coil distance that maximized its conversion efficiency over a range of lift-off distances. Wang et al. [15] explored the effects that a copper backplate, positioned between the coil and magnet at various distances from the coil, can have on the EMAT impedance, the received pulse width, and the amplitude of thickness-measurement signals. An equivalent circuit model of the receiving coil-backplate structure was established and used to predict these effects. Ding et al. [10] measured and confirmed the effect of lift-off on EMAT impedance. Zao et al. [12] explored the variation in EMAT impedance with different temperatures and developed an automatic solution, based on L-network impedance matching, to enhance signal amplitude. These works [9,10,12,15] explored the effects that one variable can have on EMAT performance; namely, the magnet-to-coil distance, the backplate distance, lift-off, and temperature. In contrast, Jian et al. [17] explored the effects of various variables on the EMAT impedance; namely, coil geometry and size, different materials samples, and various lift-off distances. It was concluded that "an EMAT must be considered as a system, including a pulse generator, a transmitting coil, and a metal sample", including all elements that can affect the equivalent inductance of the transducer. However, this work did not explore any techniques to improve EMAT performance.

### *Contribution*

In this work, a simplified impedance-matching network for EMATs is proposed and its viability for improving EMAT performance is explored. In general, previous work that studied the performance of EMATs has generally focused on optimizing the transducer's physical design for a specific application [9,10,15], or has studied the effects of different variables in the EMAT impedance, but without proposing a specific method for enhancing its performance [10,17]. Changing the physical structure of the EMAT might not be a feasible approach, especially for commercially available transducers. Zao et al. [12] proposed automatic impedance-matching networks for EMATs to improve efficiency; however, their

methodology focused on the effects of specific variables, such as temperature, rather than designing a generic automated impedance-matching system that is capable of taking various factors into account. Unlike Zao et al. [12], this work explores the application of impedance-matching networks for EMATs using different transducers at different excitation frequencies. The proposed network is tested and compared to its manual counterpart with various comparisons between the results for different frequencies and with two different transducers, demonstrating that the use of the proposed automated impedance-matching network can successfully improve the performance of EMAT systems under variable operation conditions.

## 2. Background Theory

### 2.1. Ultrasonic Waves and Electromagnetic Acoustic Transducer

Ultrasonic waves are mechanical waves that propagate through fluid or solid mediums, at a high frequency and are widely in NDT [1]. Nondestructive testing (NDT) can generally be defined as an examination, test, or evaluation performed on a test object without changing or altering that object [18]. It can be performed to assess the object's condition, usefulness, or serviceability and conditions that affect service life. NDT may also be used to measure various object characteristics, such as size, dimension, discontinuities, structure, including hardness, and grain size, among others [18]. In solids, there are longitudinal and transversal ultrasonic waves. The former presents particle motion in the same direction as the propagation of the wave, whereas the latter presents perpendicular particle motion. When they propagate across an interface between two media's, reflection and refraction occur depending on both media properties and the incident angle. To either generate or receive ultrasonic waves, a transducer and its driving electronics are required. A transducer can be broadly defined as "a device that transforms energy from one domain into another" [19]. In this context, the transducer converts energy between mechanical waves, or ultrasound, to electrical signals and vice versa [1,20].

Electromagnetic Acoustic Transducers consist of a coil underneath a permanent magnet, permanent magnet array, or electromagnet. When a current is injected into the coil, it induces a current density in the skin-depth of a conductive medium [3]. The permanent magnet generates a magnetic field that penetrates into the medium. The interaction between the current density and the magnetic field generates Lorentz forces on the surface of the medium, which is given by the cross-product

$$\mathbf{F} = \mathbf{J} \times \mathbf{B} \quad (1)$$

where  $\mathbf{J}$  is the current density,  $\mathbf{B}$  is the magnetic field, and  $\mathbf{F}$  is the resulting Lorentz force field, which, in turn, can generate ultrasonic waves directly within the medium [3,21]. Therefore, unlike conventional piezoelectric transducers, EMATs do not need physical contact with the medium under test, which is a significant advantage over traditional transducers [3,15,21]. Furthermore, depending on the magnet and coil arrangement, different types and polarization of ultrasonic waves can be generated [6–8]. In this work, spiral-coil EMATs are used.

Spiral-coil EMATs have a single permanent magnet, oriented perpendicular to the medium's surface so that the magnetic field below the EMAT is mostly perpendicular to the conductive material's surface. The spiral-coil imposes a current density generated circumferentially. The resulting Lorentz force generates a radial-polarized S-wave beneath the EMAT [3,8]. Figure 1a shows a schematic representation of a spiral-coil of EMAT. Since the main electric element of an EMAT is a coil, a simplified lumped-element model for an EMAT consists of an inductor in series with a resistor [8,10], as illustrated in Figure 1b. Other lumped-element models are possible. Notably, the inclusion of a capacitor in parallel provides a better approximation over a wide range of frequencies, as it is used by Zao et al. in [12]. Note, however, that any association between resistors, capacitors, and inductors at a given fixed frequency, can ultimately be simplified to a resistance plus a reactance, which

in the case of EMATs is positive [10], hence the model depicted in Figure 1b is consistent and it serves to give insight into the main behaviors of the transducer.

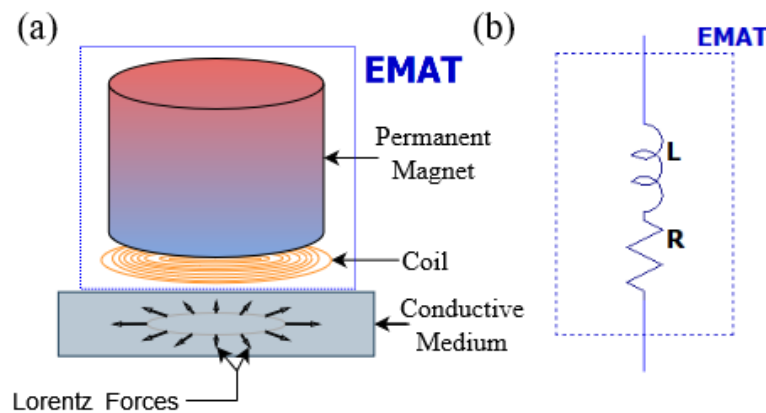


**Figure 1.** Spiral-coil EMAT. (a) Physical representation of an EMAT consisting of a spiral-coil underneath a cylindrical permanent magnet. The red section of the magnet indicates the north pole, and the blue section indicates the magnet's south pole. Lorentz forces generated are indicated by arrows inside the medium. (b) Simplified model consisting of a resistor in series with an inductor.

The pulser is responsible for generating the high-voltage signal that drives the EMAT. This pulser can be modeled as a source with an internal output impedance. Usually, the output impedance,  $Z_i$ , is equal to  $50 \Omega$  in most laboratory equipment [22]. A representation of the pulser model is shown in Figure 2. The receiver is responsible for amplifying the electric signal generated by the transducer when an ultrasonic wave is captured so it can be acquired by an oscilloscope [1].

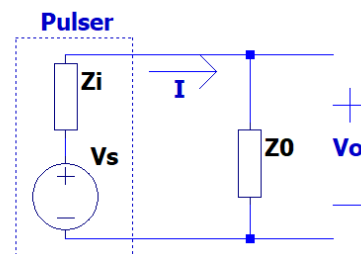


**Figure 2.** Simplified pulser model circuit where AC power is transferred from the voltage source, with voltage  $V_s$  and internal impedance  $Z_i$ , to a load of impedance  $Z_0$ . The voltage and current across the load are  $V_0$  and  $I$ , respectively.

## 2.2. Maximum Power Transfer Theorem

A model of a pulser connected to a generic load is shown in Figure 2. The pulser's output impedance and the load are represented by generic impedances,  $Z_i$  and  $Z_0$ , respectively. A generic impedance is a complex and its unit is  $\Omega$ , or Volts per Amps. The complex impedance can also be represented by the association in series of a resistance,  $R$ , and a reactance,  $X$ , which are the impedance real and imaginary parts, respectively. An association of resistors, capacitors, and/or inductors can ultimately be represented by an impedance ( $Z$ ), or by its associated resistance ( $R$ ) plus reactance ( $X$ ). To analyze the load impedance  $Z_0$ , following the model in Figure 1,  $R_0$  is the resistance of the coil and  $X_0$  its reactance, the part which is capable of storing energy that yields from the inductance ( $L$ ), and varies with frequency. The power over the load in Figure 2 is given by

$$P_0 = \frac{V_s^2}{2} \frac{R_0}{(R_i + R_0)^2 + (X_i + X_0)^2} \quad (2)$$

where  $Z_i$  is the voltage source's output impedance, which can be decomposed of its resistance  $R_i$  and reactance  $X_i$ ,  $Z_0$  is the load impedance, which can be decomposed of its resistance and reactance, respectively,  $R_0$  and  $X_0$ .  $V_s$  is the voltage value of the source. For a given  $V_s$  and  $Z_i$ , maximum power is achieved with [13,16]

$$Z_o = Z_i^*, \quad (3)$$

where the asterisk means the complex conjugate. Therefore, whenever the input impedance of a load equals the complex conjugate of the voltage source output impedance, maximum power is transferred to the load [13,16]. It is worth mentioning that the maximum power transfer theorem is stated for voltage courses, but it holds for different natures of sources provided that there exists an equivalent voltage source [23].

Assuming the source impedance as purely real, that is, a resistance, the maximum power transfer occurs when the load impedance and the source resistance are equal.

Here, the load is the EMAT, whose impedance value generally differs from the source output impedance. For this reason, one has to use some matching technique to achieve maximum power transfer [12].

### 3. Impedance-Matching Networks

#### 3.1. L-Networks

One of the simplest and most commonly used circuits for impedance matching is the L-network, which uses two lumped elements [16] that are associated with the load, changing the equivalent impedance seen by the source. To introduce a lossless network, reactive elements are required. Thus, each element can be either a capacitor or an inductor. There are two possible layouts, as shown in Figure 3. If the load resistance is greater than the source impedance, then the circuit in Figure 3a should be used as the matching network. Otherwise, one should use the circuit in Figure 3b [16].

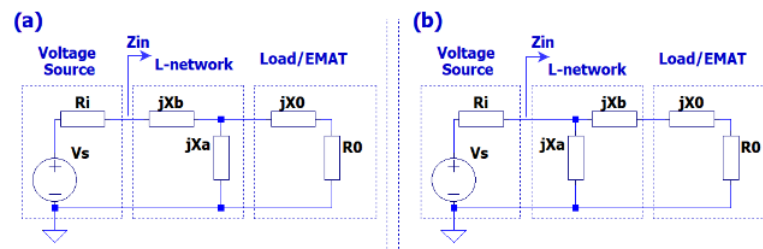


**Figure 3.** L-section matching networks. (a) Recommended network for  $R_0 > Z_i$ . (b) Recommended network for  $R_0 < Z_i$ . Where  $R_i$  and  $X_i$  are the resistance and reactance of the source, respectively, and  $R_0$  and  $X_0$  are the resistance and reactance of the load, respectively. The reactances  $X_a$  and  $X_b$  are the elements of the L-network. Here, the load represents the EMAT.  $Z_{in}$  indicates the impedance association of the L-network and the load, as seen by the source.

Considering that the EMAT impedance generally has lower resistances than the usual  $50\ \Omega$  of the source, the circuit shown in Figure 3b is adopted from here on. Further details on the EMAT impedance are provided in Section 4. The theoretical values for the reactances  $X_a$  and  $X_b$  of the L-network matching layer in Figure 1b, which ensure impedance matching and therefore maximum power transfer to the load, are

$$X_a = \frac{-(R_i^2 + X_i^2)}{QR_i + X_i}, \quad (4)$$

$$X_b = QR_0 - X_0, \quad (5)$$

where

$$Q = \pm \sqrt{\frac{R_i(1 + \frac{X_i^2}{R_i})}{R_0} - 1}. \quad (6)$$

Simplifying the assumed source output impedances, namely  $R_i = 50 \Omega$  and  $X_i = 0 \Omega$ , leads to

$$X_a = \frac{\mp 50}{\sqrt{\frac{50}{R_0} - 1}}, \quad (7)$$

$$X_b = \pm R_0 \sqrt{\frac{50}{R_0} - 1} - X_0. \quad (8)$$

where the symbol  $\pm$  refers to the sign of  $Q$  in (6).

Since the transducer impedance is not usually known a priori, and can change with a wide variety of factors, the practical approach for impedance matching consists of changing the network values  $X_a$  and/or  $X_b$  and observing the effect of the change on the power transmission. In a laboratory environment, this usually consists of an EMAT system with a matching network that can be manually adjusted through switches. A process of testing configurations until the best one is found can then be employed. The aim of this work is to automate this process.

### 3.2. Simplified One-Parallel-Element ( $X_a$ )

Here, a simplified one-element matching network is investigated. This network consists of removing the element  $X_b$  from the circuit shown in Figure 3b, keeping only  $X_a$  in parallel with the load. The resulting circuit is shown in Figure 4. With the impedance of only one element to be adjusted, it is impossible to achieve the two degrees of freedom required to perfectly match the source and the load impedance. However, one still can find the best possible value for  $X_a$ . That is, the value for  $X_a$  that maximizes the power transferred to the load under this condition. The power provided by the source is given by:

$$P = \frac{V_s^2 Z_{in}}{2Z_{in} + R_i^2}, \quad (9)$$

where  $V_s^2$  is the absolute squared value of source voltage and  $Z_{in}$  is the impedance prior to the matching network, as highlighted in Figure 4, that is

$$\frac{1}{Z_{in}} = \frac{1}{jX_a} + \frac{1}{R_0 + jX_0}, \quad (10)$$

where  $j = \sqrt{-1}$ . Because the matching network consists of reactive elements only, it does not dissipate power. Hence, maximizing the source power also maximizes the power delivered to the load, that is, the EMAT. Therefore, from

$$\frac{\partial P}{\partial X_a} = 0 \quad (11)$$

one has

$$X_a = -\frac{R_0^2 + X_0^2}{X_0}, \quad (12)$$

which differs from Equation (4). Note that  $X_a$  does not depend on the resistance of the source, as long as  $X_i$  is zero. Following the model in Figure 1, an EMAT has positive values for its resistance and reactance; therefore, the optimal value for the simplified single parallel element is negative, meaning that  $X_a$  should be a capacitor. It is worth mentioning that another simplification of the L-network is also possible, with one-series-element. However, only the one-parallel-element network is explored here, because it is simpler to fabricate.

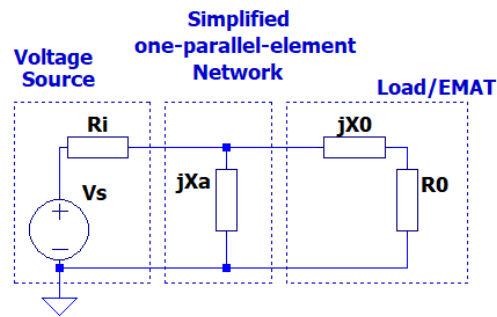


**Figure 4.** Simplified, one-parallel-element matching network, where the impedance of the source is assumed real and composed only by a resistance  $R_i$ . The load impedance is  $R_0 + jX_0$ , where  $R_0$  and  $X_0$  are the resistance and reactance of the load. The reactance  $X_a$  is the single element within the simplified matching network. Here, the load represents the EMAT. The parallel association between the simplified network and the load has total impedance  $Z_{in}$ .

#### 4. EMAT Impedance-Matching Theoretical Assessment

In order to evaluate and compare the impedance-matching networks, the circuits in Figures 3b and 4 were analyzed. The source output impedance of the Ritec RPDR-1000 OEM pulser-receiver module used is  $50 \Omega$  and the EMAT impedance was measured. With those values for  $Z_i$  and  $Z_0$ , the network's component values were theoretically calculated using the equations in Section 3.

Two different spiral-coil EMAT models were analyzed. A built-in EMAT to a Ritec RPDR-1000 OEM module, and a Sonemat EMAT model HWS2225. An impedance analyzer (Agilent model 4294A) was used to measure the impedance of the transducers placed on a 12 mm steel block, the same used in the forthcoming experimental setup. The measurement results are shown in Figure 5. It is worth mentioning the discrepancy of the results when compared to the expected constant resistance of the model presented in Figure 1b. However, precise modeling of the EMAT's impedance is not paramount in this work since it is based on automatic impedance matching, without prior knowledge of the EMAT's actual impedance.

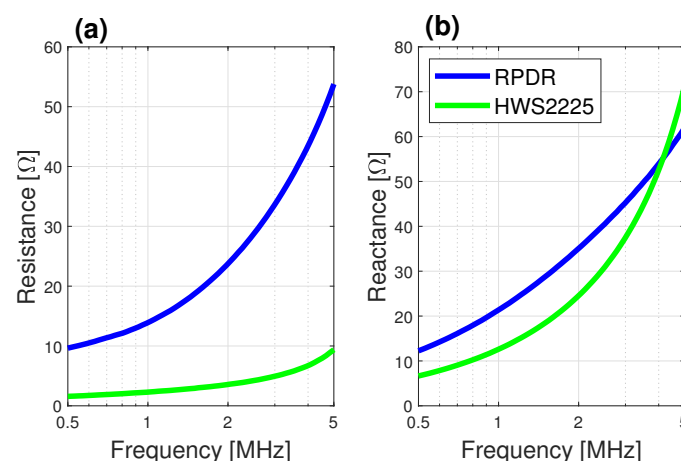


**Figure 5.** (a) Real and (b) imaginary parts of the impedance of the EMATs as a function of frequency. Blue lines are the measurements for the RPDR's included EMAT, and green lines are for the HWS2225 EMAT.

For each frequency, the respective measured EMAT impedances were used to calculate the matching network values. Then, the voltages and currents of the aforementioned circuits can also be calculated. As previously performed [24], it is possible to calculate the power across the load or transducer, which has a similar behavior to the voltage across

the transducer. Therefore, for the sake of brevity, only the voltage across the EMAT is reported hereinafter.

Figure 6a,c shows the transducer's theoretical normalized voltage as a function of frequency, (a) for the RPDR's EMAT and (c) for the EMAT model HWS2225. In both plots, it is possible to see that the natural response, without any matching network (purple line), is always lower than any other network, and the full network (blue line) provides the best voltage amplitude over the transducer, causing resonance in the steady-state sinusoidal regime which can result in a higher voltage than the normalized source. The optimal one-parallel-element (orange line) falls between the full network and no network, as expected. Furthermore, HWS2225 generally has a higher response and is more efficient than RPDR's EMAT. This is in accordance with the measurements, where the HWS2225 has a lower resistance, and a higher reactance to resistance ratio, or impedance phase. Intuitively, this means that less energy is wasted on the transducer's internal resistance. In both cases, there is a frequency where the internal resistance is greater than the source's output impedance ( $50 \Omega$ ). At this point, the solution for the full network in Figure 3b in Equations (7) and (8) is no longer possible, and above this frequency, the curve for the full network (blue line) is not plotted. This point occurs at a lower frequency for the RPDR's EMAT because of its higher resistance, namely at 4.84 MHz compared to at 8.12 MHz, for the HWS2225.

Figure 6b,d represents the matching networks component values for the calculated voltages in (a) and (c), respectively. Dashed lines represent the reactance values of components  $X_a$  and  $X_b$ , solid lines represent these values conversion to capacitances. The former has its vertical axis on the right and the latter on the left. The point where the network in Figure 3b is no longer possible is also reflected in Figure 6b,d, where the reactance for the elements of the full network (blue dashed lines) is discontinuous at 4.84 MHz or 8.12 MHz. At these points the solution for Equations (4) and (5) are discontinuous and yield purely imaginary values.

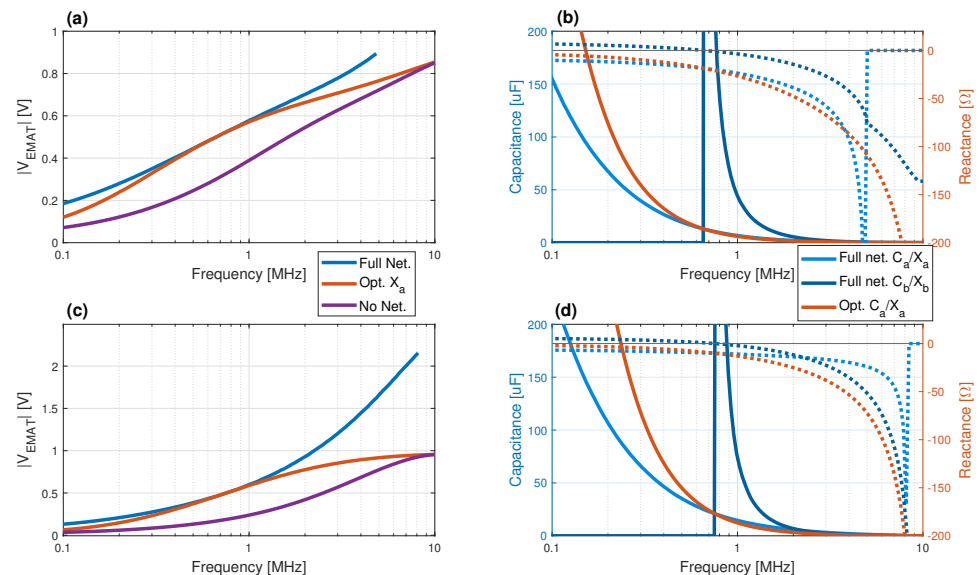


**Figure 6.** Theoretical calculations for (a) voltage across RPDR's EMAT, (b) values of the components of the matching networks of the RPDR's EMAT, (c) voltage across HWS2225's EMAT, (d) values of the components of the matching networks of the HWS2225's EMAT. For (a,c), the blue lines represents the full L-matching network, orange lines the optimum one-parallel-element ( $X_a$ ) network, and purple lines for no matching network. For (b,d), dashed lines represent the reactance values of the network's elements used in the calculations to the left, solid lines represent the respective capacitance at each given frequency. Blue lines indicate the values used in the full network evaluation, lighter shades for elements in the  $X_a$  position and darker shades for elements in the  $X_b$  position, orange lines for optimum one-parallel-element ( $X_a$ ) network.

## 5. Experimental Validation

### 5.1. Experimental Setup

As shown above, a simplified one-element network can provide a large part of the efficiency gain that can be achieved using the full network. Taking this into account, with other factors such as ease of construction, and the intended excitation frequency range, a simplified one-parallel-element ( $X_a$ ) network was chosen to be experimentally assessed, using only capacitors in the  $X_a$  position, since no inductors are needed for the one-element matching network. Capacitors are also less expensive and more readily available when compared to inductors. In order to change the capacitance value of the  $X_a$  element, a bank of eight capacitors was used with approximately binary weights. Each capacitor in the bank was connected or disconnected to the circuit so that the equivalent element  $X_a$  has a value equal to the sum of all the capacitors in the bank that are connected. It is worth mentioning that, due to the EMAT's low efficiency, high energy is required. The pulser used in all the experiments was a RPDR-100 compact EMAT pulser-receiver OEM module from Ritec, which is capable of providing up to 1000 V into a transducer.

The automatic network was assembled in a custom-made printed circuit board (PCB), and has a bank of eight film capacitors with a voltage rating of 1600 V [25] and nominal values of 0.11 nF, 0.235 nF, 0.5 nF, 1 nF, 1.95 nF, 3.4 nF, 6.0 nF, and 11.0 nF. The capacitors are switched by Metaltex AX1RC-5v relays [26]. The relays, in turn, are operated by an ESP32 microcontroller [27], which meets all the requirements for the automatic network, namely the number of digital ports and WiFi communication. The digital ports of the microcontroller, whose output is 3.3 V, could not reliably actuate the 5 V relays. Therefore, a circuit with a transducer was used to drive each relay. Apart from the capacitor bank, the network also has a 40 db attenuator, which is used to monitor the high-voltage excitation signal with an oscilloscope. The attenuator was constructed with a 2475  $\Omega$  5 W resistor from the input and another 49.9  $\Omega$  pull-down resistor. The schematic of the circuit is shown in Figure 7. The board design can be seen in Figure 8a, and a photograph of the finished board is shown in Figure 8b.

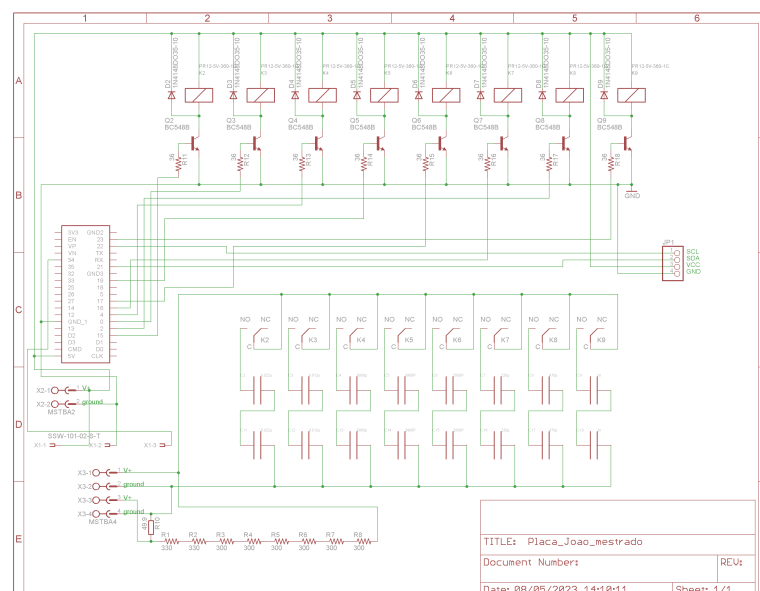


**Figure 7.** Schematic for the automatic one-parallel-element matching network board.

A similar matching network, with manual toggle switches, was also fabricated, so it can be compared to the automatic network. These networks were employed in a pulse-echo setup which is one of the main types of setups used in NDT [1]. It utilizes only one transducer, acting as both transmitter and receiver of ultrasound waves; here, both EMAT models, RPDR and HWS2225, were used positioned against a 12 mm steel block, one at a time. The analysis of the wave propagation through the medium yields its

measured characteristics. For example, thickness can be calculated from the time and the corresponding wave speed, and a flaw can be detected as it generates an echo that is received in a different time interval than the medium boundary's echo [1].

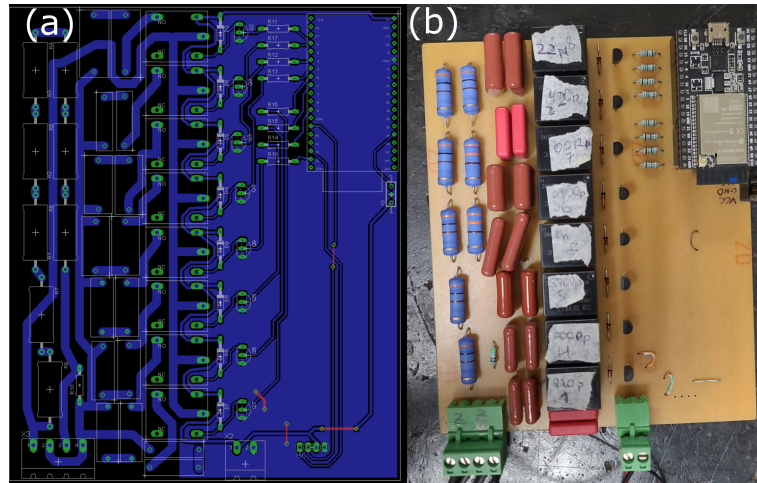


**Figure 8.** Automatic one-parallel-element matching network board. (a) PCB design made on Eagle. (b) Photograph of the finished board with all components soldered.

A simplified schematic of this experimental setup, which highlights the matching circuit, is shown in Figure 9. A detailed schematic containing all the connections between the different equipment used on the experimental setup is shown in Figure 10. It is worth mentioning that the same RPDR-100 pulser–receiver module was used for measures with both transducers. A full sweep of all the possible network values was executed, saving the waveforms of the attenuator and receiver amplifier for each configuration. A computational script running on a Linux computer was used to control the sweep. This script can send commands to the microcontroller via WiFi and request the network to change to any of the 256 ( $=2^8$ ) possible values of the capacitor bank. The scope's data is also acquired via LAN by the PC. Data were saved and later analyzed and interpreted. A function generator Tektronix model AFG3251 is used to output a 5-cycle sine tone-burst into the transmission RPDR's input port. This signal is amplified by the RPDR pulser and passes through the matching network before reaching the EMAT. At this point, the transducer generates radially polarized bulk shear ultrasonic waves which propagate within the steel block. The wave reflects at the opposite boundary of the material and the echo is received by the EMAT. The resulting signal passes through the RPDR receiver, which consists mainly of an amplifier. The scope then measures the output signal of the RPDR receiver, and also the signal at the matching network's attenuator. That is, the scope monitors the signal that goes into and out of the EMAT.

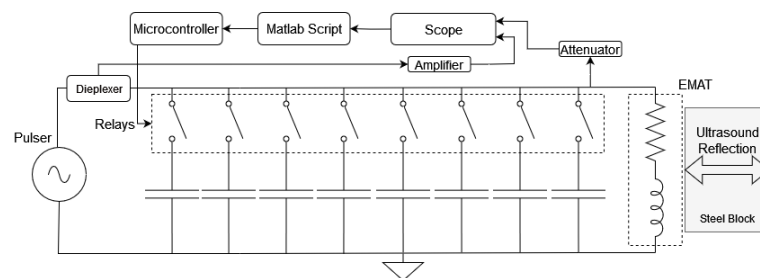


**Figure 9.** A simplified schematic of the experimental setup, which highlights the circuit composed of the pulser, matching networks, and load; in this case, the EMAT.

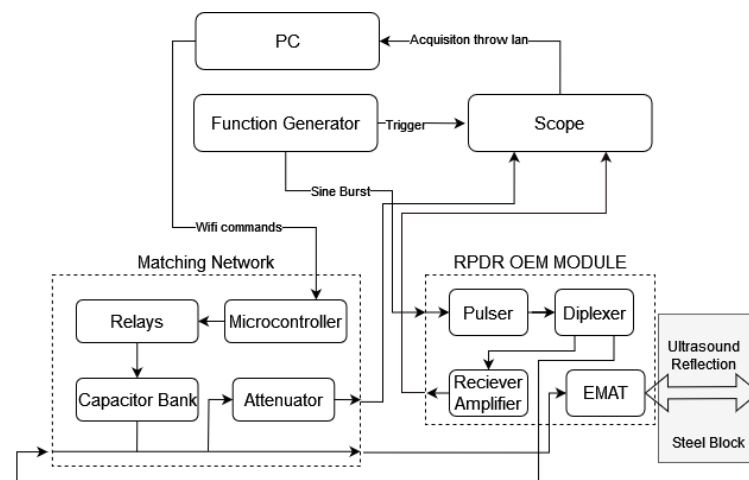


**Figure 10.** Pulse-echo setup schematic with the equipment and connections used in the experimental bench.

### Hardware Peak Detector

In order to speed up the process and make a fully automated network, a peak detector that feeds information directly to the microcontroller was used. Therefore, the oscilloscope and PC are no longer needed. The main goal of this work is to fabricate a convenient-to-use matching network to be connected between the pulser and the transducer that does not require any other connections in order to provide the optimal matching configuration. The oscilloscope was used in this experiment exclusively to save the data for post-analysis.

The peak detector is connected to the output of the attenuator and its value is read by an external analog-to-digital converter (ADC) model ADS1015 [28], as the microcontroller's internal analog readers were experimentally deemed inconsistent for this application and the ADS1015 was readily available. The peak detector circuit is shown in Figure 11, and was based on [29]. The circuit works by storing the highest input value in the capacitor (C1). A diode (D1) is used to remove the negative parts of the input which then passes through an operational amplifier (opamp, U1) which acts mainly as a buffer, and then, through another diode (D2), the capacitor is charged. This second diode guarantees the capacitor does not discharge when the signal falls since it becomes reverse-biased. The second opamp (U2) is configured as a voltage follower, providing the output of the circuit which is the same as the voltage across the capacitor. To discharge the capacitor, a resistor (R4) is used in parallel to it. This resistor's value regulates the rate of discharge. In this circuit, an NPN transistor was used in series with R4 so that the signal label 'Control' can determine whether and when the peak detector is discharged.

The timing of the peak detector's reading needs to be considered. In this case, the sine tone burst excitation signal can last from 1.25 to 5  $\mu$ s and causes interference. If the peak detector's output was built to discharge over time, the ADC reading would need to be right after the sine tone burst, when this value is maximum. The ADC's reading is requested by the microcontroller via I2C protocol [30], and takes at least 6 ms. This is not fast enough to guarantee a reading at the right time simply by polling the ADS. Therefore, the peak detector is not discharged over time, and a transducer is used so that the microcontroller can control when it is discharged, doing so quickly, before the next tone burst excitation signal is triggered. To be able to do this, the microcontroller was programmed with a digital port *interrupt*, using the function generator's *interrupt* rising edge, as a general synchronization signal. It is worth mentioning that a low-pass filter was also used to connect the trigger to the microcontroller's *interrupt* to avoid the bang's interference, which would result in many rising edges in the trigger signal and various subsequent *interrupts*. To eliminate the connection between the function generator and the microcontroller, it can also be replaced by a comparator activating the microcontroller's *interrupt* by using the peak detector's

signal rise. After the *interruption*, the microcontroller waits 10 ms to request the ADC's reading. After the reading is saved, the microcontroller discharges the peak detector.

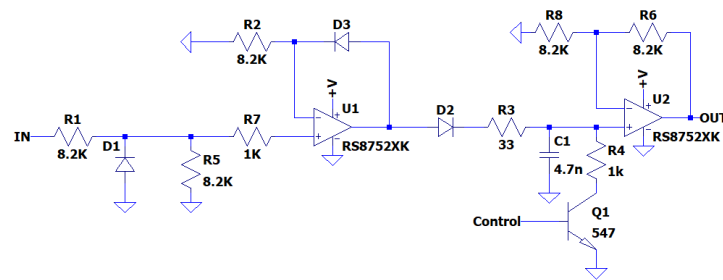


**Figure 11.** Peak detector circuit based on the ‘Improved Peak Detector’ [29]. In this setup, the input ‘IN’ node connects to the matching network’s attenuator, the output ‘OUT’ connects to the ADC, and the ‘CONTROL’ node connects to a digital output in the microcontroller.

Figure 12 shows the signals for the attenuator’s output, which is the peak detector’s input, the peak detector’s output, and the trigger. Figure 12a,b shows these signals at a time scale where the bang’s interference can be seen. Figure 12c shows the same signals at a wider time scale, where the discharge of the peak detector can be seen. The bang and its interference cannot be seen in Figure 12c due to its short duration and the long time between samples in this wider time scale. The detailed schematic of this setup including the peak detector is shown in Figure 13.

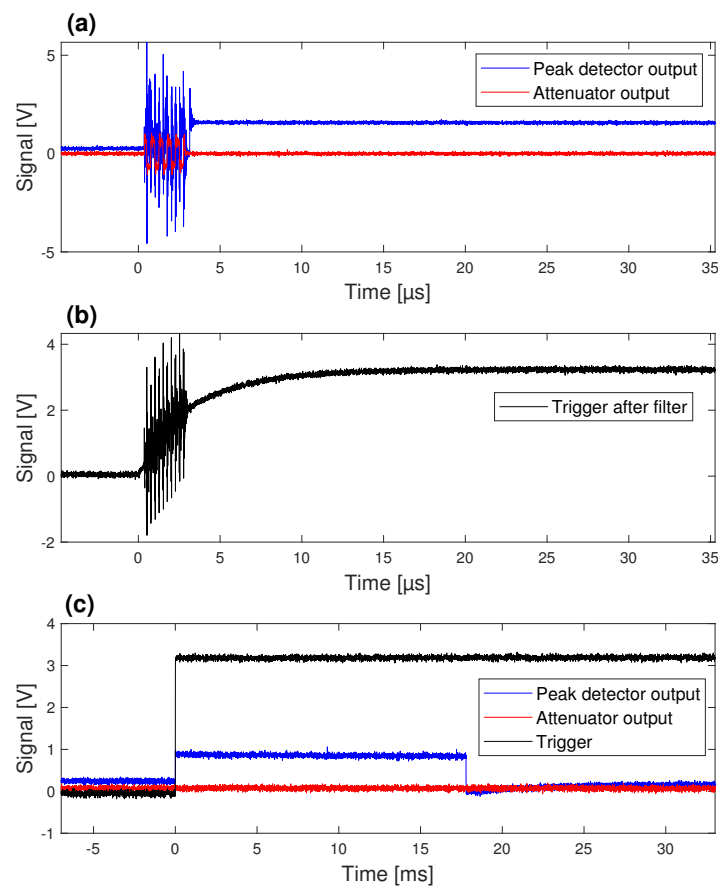


**Figure 12.** Signals measured with an oscilloscope: (a) shows the peak detector’s input (attenuator’s output) in blue, and its output in red; (b) shows the trigger signal from the function generator after passing through the low-pass filter in black. Both (a,b) have the same time-scale; (c) shows the three signals mentioned previously using the same colors, at a wider time scale.

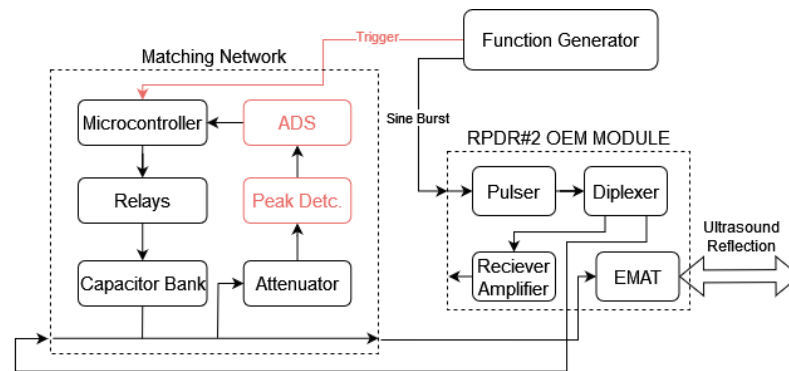


**Figure 13.** Schematic of the experimental setup for the pulse-echo with peak detector. The main differences from the schematic in Figure 10 are highlighted in red.

### 5.2. Experimental Results

Here, the results were captured in the first experimental setup, which does not use the hardware peak detector. Figure 14 shows the peak-to-peak amplitude of the transmitted signal at the RPDR's EMAT as a function of the equivalent capacitance for each capacitor bank configuration evaluated. This amplitude is shown for the three excitation frequencies; namely, 2 MHz, 3 MHz, and 4 MHz, comparing the manual experimental results, automatic experimental results, and the theoretical values. The experimental capacitance for optimal matching is slightly higher than the theoretical one. Good agreement was obtained between the manual experimental method results, the automatic experimental method results, and the theoretical values. It is worth mentioning that the theoretical calculation is assumed as a CW sinusoidal excitation, whereas the experimental setup uses a 5-cycle tone burst operation, which therefore presents a finite bandwidth, and then differences between them can be expected. There are also a variety of common non-ideal effects that affect the experimental results, such as impedance of the cables or electromagnetic interference.

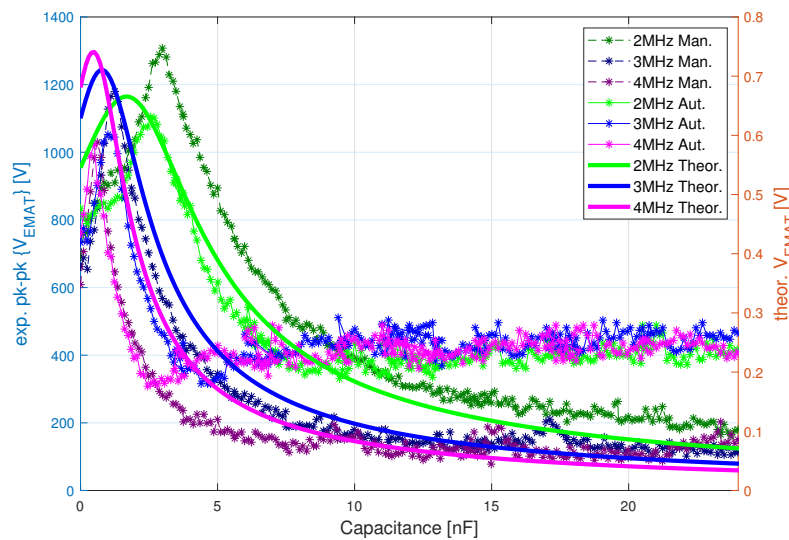


**Figure 14.** Peak-to-peak amplitude at the RPDR's EMAT as a function of the resultant capacitance of the capacitor bank. Experimental results obtained with manual impedance matching are in dashed darker lines, and the results obtained with the automatic method are in solid brighter lines, both marked with asterisks that have their vertical axis on the left. Theoretical amplitudes for the voltage across the transducer are shown in wider, unmarked, solid lines with the vertical axis on the right. Three excitation frequencies were evaluated—2, 3, and 4 MHz—represented by green, blue, and magenta lines, respectively.

Figure 15 shows the waveforms for the no-network and optimum network for the 2 MHz excitation frequency at the RPDR EMAT. Each point of Figure 14 was derived from a similar waveform. Finally, for each frequency and matching network used, the values for optimal capacitance, peak-to-peak voltage, gain, and time taken to do the full sweep can be found in Table 1. We can see that both manual and automatic methods have similar optimal capacitances for each frequency. The manual results are slightly higher than the automatic ones. The automatic network takes considerably less time to complete the full sweep.

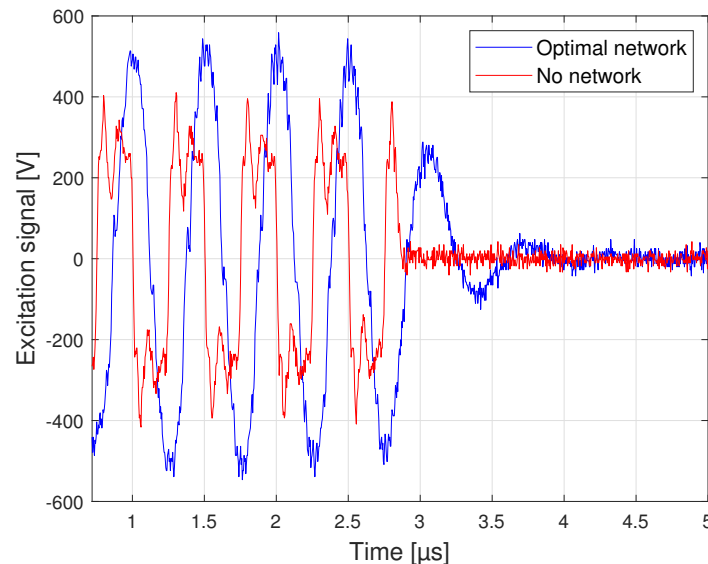


**Figure 15.** Optimal matching network (blue line) effect at 2 MHz on excitation signal, compared to the signal without any matching network (red line). Resulting voltage at the RPDR's transducer.

**Table 1.** Results for the pulse-echo experimental setup using RPDR's EMAT.

	Optimal Capacitance Found [nF]	No Network pk-pk [V]	Optimal Network pk-pk [V]	Gain [db]	Time for Full Sweep [s]
2 MHz Man.	3.06	691.5	1307.9	5.5352	1481.9
3 MHz Man.	1.235	661.4	1180.1	5.0283	1372.7
4 MHz Man.	0.61	608.8	1029.7	4.5647	1241.7
2 MHz Aut.	2.56	834.4	1104.9	2.4386	754.4
3 MHz Aut.	1.0	732.8	1052.3	3.1424	719.3
4 MHz Aut.	0.50	759.1	1022.2	2.5843	718.3

Figure 16 shows the peak-to-peak amplitude of the transmitted signal at the HWS2225 EMAT as a function of the equivalent capacitance for each capacitor bank configuration evaluated and a comparison between the experimental results and the theoretical calculations. Similar to the RPDR EMAT's results, shown in Figure 14, here one is also affected by those same experimental factors that render experimental measures slightly different from the theoretical one. Nonetheless, due to the HWS2225's higher efficiency, the capacitance at which both methods' maxima occur has a high degree of agreement. Summarized results can be found in Table 2.

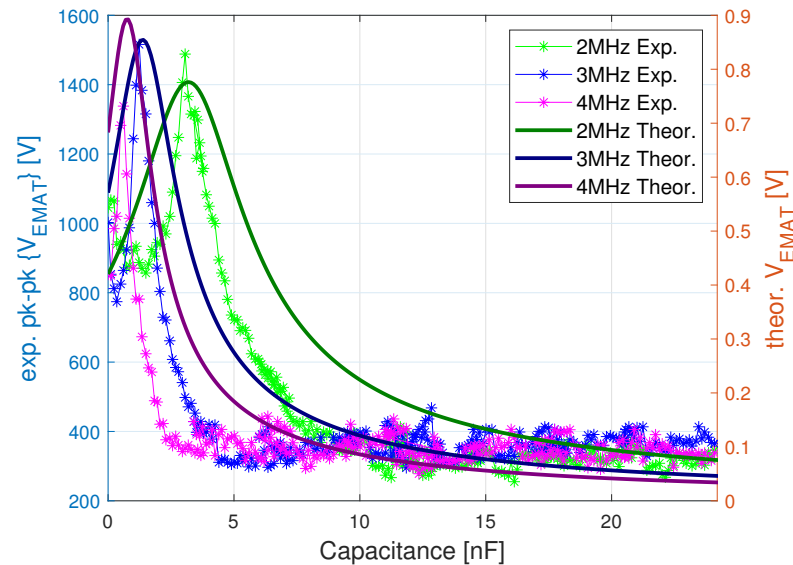


**Figure 16.** Peak-to-peak amplitude at the Sonemat’s HWS2225 EMAT as a function of the resultant capacitance of the capacitor bank. Experimental results with the automatic method are brighter lines marked with asterisks that have their vertical axis on the left. Theoretical amplitudes for the voltage across the transducer are shown in wider, darker, unmarked lines with the vertical axis on the right. Three excitation frequencies were evaluated—2, 3, and 4 MHz—represented by green, blue, and magenta lines, respectively.

**Table 2.** Results for the pulse-echo experimental setup using HWS2225.

	Optimal Capacitance Found [nF]	No Network pk-pk [V]	Optimal Network pk-pk [V]	Gain [db]
2 MHz Aut.	3.06	1045.1	1488.1	3.0698
3 MHz Aut.	1.235	1002.5	1515.9	3.5917
4 MHz Aut.	0.61	852.2	1338.1	3.9191

#### Hardware Peak Detector

Figure 17 shows the peak-to-peak amplitude of the transmitted signal as a function of the equivalent capacitance for each capacitor bank configuration evaluated. Unlike in Figures 14 and 16, these values were not generated from a waveform captured by the oscilloscope, they were captured by the ADS from the peak detector and saved by the microcontroller. For each frequency, the peak-to-peak voltage with no network, the highest voltage value found, as well as its corresponding capacitance and gain can be found in Table 3. The table is divided for each of the two transducers used. At 2 MHz using the HWS2225 due to the transducer’s higher efficiency, the peak detector was saturated. To solve this, the function generator’s output was lowered from the standard 10 V to 8.3 V. This measurement with lower power yielded consistent results and can be seen in Figure 17b, in the darker green line, labeled as ‘2 MHz LP’.

The time taken to perform the full sweep depends only on the number of measurements, the average chosen, and the trigger interval set on the function generator, in this case, the values were 256, 4, and 200 ms, respectively. This yields the full sweep time of  $((256 \times 4) + 1) \times 0.2 = 205$  s. After all the measurements are taken, the microcontroller automatically calculates and switches the network to the optimum capacitance, hence the plus one cycle needed on the full sweep time.

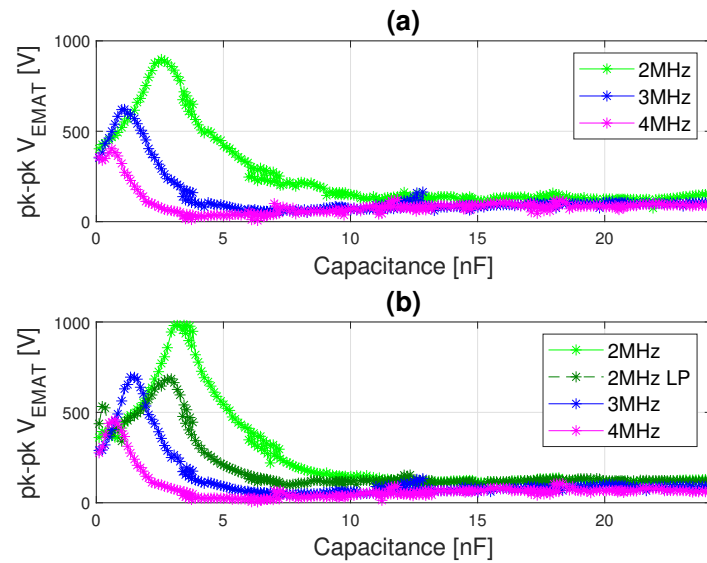


**Figure 17.** Peak-to-peak voltage, measured by the hardware peak detector across (a) RPDR's transducer, (b) HWS2225. Three excitation frequencies were evaluated—2, 3, and 4 MHz—represented by green, blue, and magenta lines, respectively. The darker green line in the bottom graph labeled '2MHz LP' was obtained with lower power to avoid saturation in the peak detector, the normal 10 V excitation from the function generator was switched to 8.3 V just for this measure.

**Table 3.** Results for the pulse-echo using hardware peak detector for both transducers. It can be observed that the cases in which the unmatched transducer's impedance value is further from the source's impedance require a higher capacitance to match, and the matching provides a higher gain. The HWS2225 transducer, at lower frequencies, benefits the most from the one-parallel-element matching network.

	RPDR's EMAT				HWS2225			
	Optimum Capacitance Found [nF]	No Network pk-pk [V]	Optimal Network pk-pk [V]	Gain [db]	Optimum Capacitance Found [nF]	No Network pk-pk [V]	Optimal Network pk-pk [V]	Gain [db]
2 MHz Aut.	2.45	402.9	897.15	6.9533	2.795	360.75	981.75	8.6958
3 MHz Aut.	1	352.65	621.15	4.9170	1.235	289.5	694.8	7.6042
4 MHz Aut.	0.5	356.7	403.35	1.0675	0.61	276	459	4.4180

## 6. Conclusions

Electromagnetic acoustic transducers are essential devices in several ultrasonic applications, but they have low efficiency. Therefore, it is vital to use an impedance-matching network in order to increase its signal-to-noise ratio. Impedance matching can be time-consuming and depends on various factors that often change during laboratory testing or field applications, such as the transducers, the excitation frequency, and the lift-off, among others. Therefore, automation of the impedance-matching process can be of great benefit to the use of EMATs. In this paper, a simplified one-element impedance-matching network was proposed and its optimal values were theoretically derived. Two models of spiral-coil EMAT were evaluated and their full bandwidth was determined, comparing the performance of the simplified network to a full L-network. Depending on the intended excitation frequency, the one-element network can provide a large part of the performance of the full L-network. The one-element network also works better in a wide range of frequencies because it is not necessary to change its layout or the type of component, requiring only capacitors and no inductors. An automatic matching network was designed and

fabricated. The resulting experimental curves of voltage across the EMAT as a function of the network's capacitance were compared to the theoretical ones for three distinct excitation frequencies with two transducers. The automatic matching process proved to be effective. Compared to the non-matched setup, the automatic impedance-matching network provided from 2.6 to 5.6 dB gain in the RPDR's EMAT voltage signal and from 3.0 to 3.9 dB in the HWS2225 EMAT's signal, which is naturally more efficient. The main advantage of the automatic network is the confidence that the best configuration for each setup can be used.

**Author Contributions:** Conceptualization, A.C.K. and J.P.T.A.; methodology, J.P.T.A., P.L.F.C.B., V.S.M. and A.C.K.; software, J.P.T.A., P.L.F.C.B., V.S.M. and A.C.K.; validation, J.P.T.A., P.L.F.C.B., V.S.M. and A.C.K.; formal analysis, J.P.T.A. and A.C.K.; investigation, J.P.T.A., P.L.F.C.B., V.S.M. and A.C.K.; resources, A.C.K.; data curation, J.P.T.A.; writing—original draft preparation, J.P.T.A.; writing—review and editing, V.S.M. and A.C.K.; visualization, J.P.T.A.; supervision, A.C.K. and V.S.M.; project administration, A.C.K.; funding acquisition, A.C.K. All authors have read and agreed to the published version of the manuscript.

**Funding:** This study was financed in part by the Coordenação de Aperfeiçoamento de Pessoal de Nível Superior—Brasil (CAPES) Finance Code 001, by the Carlos Chagas Filho Foundation for Research Support of Rio de Janeiro State (FAPERJ), Brazil, and by the Brazilian National Council for Scientific and Technological Development, CNPq.

**Institutional Review Board Statement:** Not applicable.

**Data Availability Statement:** The data presented in this study are available on request from the corresponding author.

**Acknowledgments:** I thank the team at Research Center for Inspection Technology, who helped with the work, especially Lucas Monteiro Martinho, Rafael Honório, and Rodrigo Guerato.

**Conflicts of Interest:** The authors declare no conflict of interest. The funders had no role in the design of the study; in the collection, analyses, or interpretation of data; in the writing of the manuscript; or in the decision to publish the results.

## References

1. Schmerr, L.W. *Fundamentals of Ultrasonic Nondestructive Evaluation: A Modeling Approach*; Springer: Berlin/Heidelberg, Germany, 2016.
2. Kubrusly, A.C.; Dixon, S. Application of the reciprocity principle to evaluation of mode-converted scattered shear horizontal (SH) wavefields in tapered thinning plates. *Ultrasonics* **2021**, *117*, 106544. [[CrossRef](#)] [[PubMed](#)]
3. Hirao, M.; Ogi, H. *EMATs for Science and Industry: Noncontacting Ultrasonic Measurements*; Springer: Berlin/Heidelberg, Germany, 2017.
4. Rose, J.L. *Ultrasonic Guided Waves in Solid Media*; Cambridge University Press: Cambridge, UK, 2014.
5. Cheeke, J.N.D. *Fundamentals and Applications of Ultrasonic Waves*, 2nd ed.; CRC Press: Boca Raton, FL, USA, 2017.
6. Miao, H.; Li, F. Shear horizontal wave transducers for structural health monitoring and nondestructive testing: A review. *Ultrasonics* **2021**, *114*, 106355. [[CrossRef](#)] [[PubMed](#)]
7. Rose, J.L.; Jiao, D.; Spanner, J. Ultrasonics Guided Waves for Piping Inspection. In *Review of Progress in Quantitative Nondestructive Evaluation*; Thompson, D.O., Chimenti, D.E., Eds.; Springer: Boston, MA, USA, 1997; Volume 16A, pp. 1285–1290.
8. Maxfield, Z.W.B. Electromagnetic Acoustic Transducers for Nondestructive Evaluation. In *ASM Handbook, Volume 17: Nondestructive Evaluation of Materials*; Ahmad, A., Bond, L.J., Eds.; ASM International: Novelt, OH, USA, 2018.
9. Wu, Y.; Wu, Y. The Effect of Magnet-to-Coil Distance on the Performance Characteristics of EMATs. *Sensors* **2020**, *20*, 5096. [[CrossRef](#)] [[PubMed](#)]
10. Ding, X.; Hong, B.; Wu, X.; He, L. Lift-off Performance of Receiving EMAT Transducer Enhanced by Voltage Resonance. In Proceedings of the 18th World Conference on Nondestructive Testing, Durban, South Africa, 16–20 April 2012.
11. Wenze, S.; Chen, W.; Lu, C.; Zhang, J.; Chen, Y.; Xu, W. Optimal Design of Spiral Coil EMATs for Improving Their Pulse Compression Effect. *J. Nondestruct. Eval.* **2021**, *40*, 38.
12. Zao, Y.; Ouyang, Q.; Zhang, X.; Hou, S.; Fang, M. The dynamic impedance matching method for high temperature electromagnetic acoustic transducer. In Proceedings of the 2017 29th Chinese Control and Decision Conference (CCDC), Chongqing, China, 28–30 May 2017; pp. 1923–1927.
13. Kong, C. A general maximum power transfer theorem. *IEEE Trans. Educ.* **1995**, *38*, 296–298. [[CrossRef](#)]
14. Kuang, Y.; Jin, Y.; Cochran, S.; Huang, Z. Resonance tracking and vibration stabilization for high power ultrasonic transducers. *Ultrasonics* **2014**, *54*, 187–194. [[CrossRef](#)] [[PubMed](#)]

15. Wang, J.; Wu, X.; Song, Y.; Sun, L. Study of the Influence of the Backplate Position on EMAT Thickness-Measurement Signals. *Sensors* **2022**, *12*, 8741. <https://doi.org/10.3390/s22228741>. [CrossRef] [PubMed]
16. Pozar, D.M. *Microwave Engineering*, 4th ed.; University of Massachusetts at Amherst: Amherst, MA, USA, 2012; Chapters 2.6 and 5.1.
17. Jian, X.; Dixon, S.; Edwards, R.; Morrison, J. Coupling mechanism of an EMAT. *Ultrasonics* **2006**, *44*, e653–e656. [CrossRef] [PubMed]
18. Chuck, H. *Handbook of Nondestructive Evaluation*, 2nd ed.; McGraw Hill Professional: New York, NY, USA, 2012.
19. Sekhar, P.; Uvizy, V. 2—Review of sensor and actuator mechanisms for bioMEMS. In *MEMS for Biomedical Applications*; Bhansali, S., Vasudev, A., Eds.; Woodhead Publishing: Sawston, UK, 2012; pp. 46–77.
20. Kuperman, W.A. Underwater Acoustics. In *Encyclopedia of Physical Science and Technology*, 3rd ed.; Meyers, R.A., Ed.; Academic Press: Cambridge, MA, USA, 2003; pp. 317–338.
21. Ribichini, R. Modelling of Electromagnetic Acoustic Transducers. Ph.D. Thesis, Imperial College London, London, UK, 2011.
22. Allam, A.; Bhardwaj, A.; Sabra, K.; Erturk, A. Piezoelectric transducer design and impedance tuning for concurrent ultrasonic power and data transfer. In *Active and Passive Smart Structures and Integrated Systems XVI*; Han, J.H., Shahab, S., Yang, J., Eds.; Society of Photo-Optical Instrumentation Engineers (SPIE) Conference Series; SPIE: Long Beach, CA, USA, 2022.
23. Agarwal, A.; Lang, J.H. *Foundations of Analog and Digital Electronic Circuits*; Morgan Kaufmann Publishers: San Francisco, CA, USA, 2005.
24. Torres de Sousa Andrade, J.P.; Suzano Medeiros, V.; Kubrusly, A.C. A simplified automatic impedance matching network for electromagnetic acoustic transducers. In Proceedings of the 2023 7th International Symposium on Instrumentation Systems, Circuits and Transducers (INSCIT), Rio de Janeiro, Brazil, 28 August–1 September 2023; pp. 1–6. [CrossRef]
25. Metallized Polypropylene Film Capacitors ECWH(A) Series. Available online: <https://industrial.panasonic.com/cdbs/ww-data/pdf/RDI0000/ABD0000C187.pdf> (accessed on 12 July 2023).
26. Metaltex Miniature Relay. Available online: <https://www.metaltex.com.br/assets/produtos/pdf/ax.pdf> (accessed on 2 May 2023).
27. ESP32-WROVER-I and ESP32-WROVER-IE Datasheet. Available online: [https://www.espressif.com/sites/default/files/documentation/esp32-wrover-e\\_esp32-wrover-ie\\_datasheet\\_en.pdf](https://www.espressif.com/sites/default/files/documentation/esp32-wrover-e_esp32-wrover-ie_datasheet_en.pdf) (accessed on 25 January 2023).
28. Ultra-Small, Low-Power, 12-Bit Analog-to-Digital Converter with Internal Reference. Available online: <https://cdn-shop.adafruit.com/datasheets/ads1015.pdf> (accessed on 30 April 2023).
29. Kelley, H.; Alonso, G. LTC6244 High Speed Peak Detector. Available online: <https://www.analog.com/en/technical-articles/ltc6244-high-speed-peak-detector.html> (accessed on 2 May 2023).
30. Irazabal, J.; Blozis, S. Application Note AN10216-01 I2C Manual. 2003. Available online: <https://www.nxp.com/docs/en/application-note/AN10216.pdf> (accessed on 13 July 2023).

**Disclaimer/Publisher’s Note:** The statements, opinions and data contained in all publications are solely those of the individual author(s) and contributor(s) and not of MDPI and/or the editor(s). MDPI and/or the editor(s) disclaim responsibility for any injury to people or property resulting from any ideas, methods, instructions or products referred to in the content.